Symmetric Cell Electrochemical Impedance Spectroscopy of $Na_2FeP_2O_7$ Positive Electrode Material in Ionic Liquid Electrolytes

Jinkwang Hwang,[†] *Kazuhiko Matsumoto,*[*,†,‡] *and Rika Hagiwara*[†,‡]
[†]Graduate School of Energy Science, Kyoto University, Yoshida-honmachi, Sakyo-ku, Kyoto 606-8501, Japan
[‡]Unit of Elements Strategy Initiative for Catalysts & Batteries (ESICB), Kyoto University, Katsura, Kyoto 615-8510, Japan

*Corresponding author: Kazuhiko Matsumoto
E-mail: k-matsumoto@energy.kyoto-u.ac.jp
Tel: +81757534817
Fax: +81757535906

ABSTRACT

Symmetric cell electrochemical impedance spectroscopy (SCEIS) is a powerful method to analyze electrode materials for secondary batteries. The EIS results are used to obtain information related to electrochemical processes such as charge-transfer resistance. In this study, SCEIS is employed to investigate the electrochemical performance of the $Na_2FeP_2O_7$ positive electrode for sodium secondary batteries operating at temperatures ranging from room to intermediate temperatures using the ionic liquid (IL) electrolytes, Na[FSA]-[C_2C_1im][FSA] (IL_{FSA}) (C_2C_1im = 1-ethyl-3-methylimidazolium, FSA = bis(fluorosulfonyl)amide). The obtained SCEIS for Na metal, acetylene black, α-Al_2O_3, and V_2O_5 revealed that the resistance of the high-frequency region in the Nyquist plots is a combination of several factors (the Na[FSA] fraction, ionic conductivity of the electrolyte, and electronic conductivity of the composite electrode). The activation energies obtained by the Arrhenius plots for both the high-frequency and charge-transfer resistance of $Na_2FeP_2O_7$/IL_{FSA}/$Na_2FeP_2O_7$ SCEIS showed that a significant decrease in the charge-transfer resistance contributes to the high rate performance in the intermediate temperature range.

1. INTRODUCTION

Global energy issues associated with economic and environmental problems have driven the development of sodium secondary batteries as candidates for post-lithium secondary batteries. These batteries are particularly suitable for large-scale applications owing to their low cost and the high abundance of sodium resources.[1-4] Many researchers have made efforts to improve the electrochemical performance and safety of sodium secondary batteries.[2-3, 5-6] Recent intensive research studies have greatly improved the materials used for sodium secondary batteries.[1-8] A number of positive electrode materials (layered metal oxide, polyanionic, Prussian blue, etc.) and negative electrode materials (metal alloy, hard carbon, phosphide, etc.) for sodium secondary batteries have been reported to show outstanding electrochemical performance with high energy and power densities.[1-4, 6-9] Although the use of organic electrolytes has been the major choice in these studies thus far, the number of studies investigating the use of ionic liquids (ILs) has increased with the aim of establishing safer sodium secondary batteries.[10-17] The high thermal stability of ILs also enables them to be used at elevated temperatures; in fact, our recent studies revealed that the intermediate-temperature operation of sodium secondary batteries enhances the performance of electrode materials, including $NaCrO_2$, $Na_2FeP_2O_7$, $NaFePO_4$, $Na_3V_3(PO_4)_3$, Sn-alloy, hard carbon, and phosphide, without causing safety problems. In particular, rate performance was dramatically enhanced due to elevating operation temperatures.[18-25]

Electrochemical impedance spectroscopy (EIS, which denotes electrochemical impedance spectrum hereafter) is a powerful tool that enables fast and simple analysis of the physicochemical and electrochemical characteristics of batteries.[26-30] The simplest and most effective way to obtain EIS measurements of batteries in the laboratory is to use a coin-type half-cell. The EIS results are

normally interpreted by using a Nyquist or Bode plot.[31-33] Half-cell EIS provides information about both the working and counter electrodes, and separation of the information relating to these two electrodes is often difficult. This difficulty is particularly significant for sodium secondary batteries with IL electrolytes, because they show the very large impedance of the film on Na metal.[34-35] On the other hand, Symmetric cell electrochemical impedance spectroscopy (SCEIS) measurements using two identical electrodes at the same state-of-charge (SOC) directly renders the data of the corresponding electrode without being adversely affected by the effects of the counter electrode. This approach is thus a preferable method to investigate electrode materials, especially for IL electrolytes, for the above-mentioned reason. However, the interpretation of SCEIS results has not been sufficiently studied, particularly for sodium secondary batteries with IL electrolytes.

This paper presents our study of the effects of the operating temperature on sodium secondary batteries with IL electrolytes using SCEIS with nine different types of electrode constituents (active and additive materials), by taking the performance of the $Na_2FeP_2O_7$ electrode as an example. The pyrophosphate, $Na_2FeP_2O_7$, is one of the well-studied positive electrode materials for sodium secondary batteries. The material exhibits stable charge-discharge performance using organic electrolytes and IL electrolytes, and very high rate capability was achieved using IL electrolytes at intermediate temperatures.[19, 36-42]

In this study, EIS was performed at four different temperatures (298, 323, 343, and 363 K) using the Na[FSA]-[C_2C_1im][FSA] (C_2C_1im = 1-ethyl-3-methylimidazolium) IL system (IL_{FSA}) [12, 34] with x(Na[FSA]) in a molar ratio ranging from 0.1 to 0.5. Thereby, we aimed to obtain the fundamental information pertaining to our previous results, which indicated a high rate capability for the positive and negative electrodes at elevated temperatures.[18-19, 24] Origins of the

resistance appearing in the high-frequency region (R_h) are also investigated because it significantly contributes to electrode performance. The results are discussed by considering the bulk and charge-transfer resistance (R_{bulk}, R_h, and R_{ct}).

2. Experimental Section

2.1. Preparation of Electrodes for Symmetric Cells.

Sodium metal (Sigma-Aldrich chemistry, purity 99.95%) was cut into a disk (16 mm in diameter) and fixed to an Al plate current collector as the electrode. Aluminum mesh (Nilaco Corporation) was cut into a disk (13 mm in diameter) for use as the electrode. AB (Wako Pure Chemical Industries) electrodes were prepared by mixing AB with PTFE in four different weight ratios (AB:PTFE = 95:5, 50:50, 5:95, and 100:0 wt%). Each of these combinations was mixed in a mortar and pestle and the resulting mixtures were spread out to form a sheet. The respective sheets were pressed onto an Al mesh to obtain a loading mass of approximately 3 mg cm^{-2}. For the100% AB electrode, AB was pelletized (70 MPa) for 10 min. The electrodes of α-Al_2O_3 (Wako Pure Chemical Industries) and V_2O_5 (Sigma-Aldrich Chemistry, purity 99.6%) were prepared in the same manner as the AB/PTFE electrodes. The $Na_2FeP_2O_7$ sample was prepared in the same manner as previously reported,[19, 42] and the electrodes were prepared in the same manner as the AB/PTFE electrodes. The morphologies of V_2O_5 and α-Al_2O_3 and the microstructures of the $Na_2FeP_2O_7$ electrodes were observed by field-emission scanning electron microscopy (FE-SEM, Hitachi SU-8020). (See Figure S1, S3, and S5, respectively.) EDS mapping was performed using an analyzer (Horiba EMAXEvolution X-max) attached to the SEM. XRD patterns of V_2O_5 and α-Al_2O_3, and $Na_2FeP_2O_7$ were collected in the Bragg–Brentano geometry using a Rigaku SmartLab

diffractometer with Ni-filtered Cu-*K*α radiation (40 kV and 30 mA). (See supporting information for details. Figure S2, S4, and S5, respectively)

The salts, Na[FSA] (Mitsubishi Materials Electronic Chemicals, purity > 99%) and [C_2C_1im][FSA] (Kanto Chemical, purity > 99.9%), were dried under vacuum for 24 hours at 353 K. A glass microfiber filter (Whatman GF/A) was impregnated with the electrolyte at 333 K under vacuum for 24 hours prior to the assembly of the test cell.

2.2 Electrochemical Measurement.

The charge-discharge measurements to control the SOC of the electrode materials were carried out using 2032 coin-type cells and a HJ1001SD8 charge-discharge test device (Hokuto Denko). The $Na_2FeP_2O_7$ electrodes at SOC = 50% and 0% were prepared by fully charging the cells and discharging them to SOC = 50% or 0% at 0.1C (Figure 1). The symmetric cells for EIS were prepared using 2032 coin-type cells using the electrodes above (at a specific SOC). The cells were assembled under dry Ar atmosphere in a glove box. The EIS measurements were performed with a VSP potentiostat (Bio-Logic) at 298, 323, 343, and 363 K over a frequency range from 1 mHz or 100 mHz to 100 kHz with an ac amplitude of 10 mV. All the measurements were performed at least 1 h after temperature adjustment in an ESPEC thermostatic chamber. The EIS parameters were fitted using EC-Lab software.

3. RESULTS AND DISCUSSION
3.1. SCEIS and Nyquist Plots.

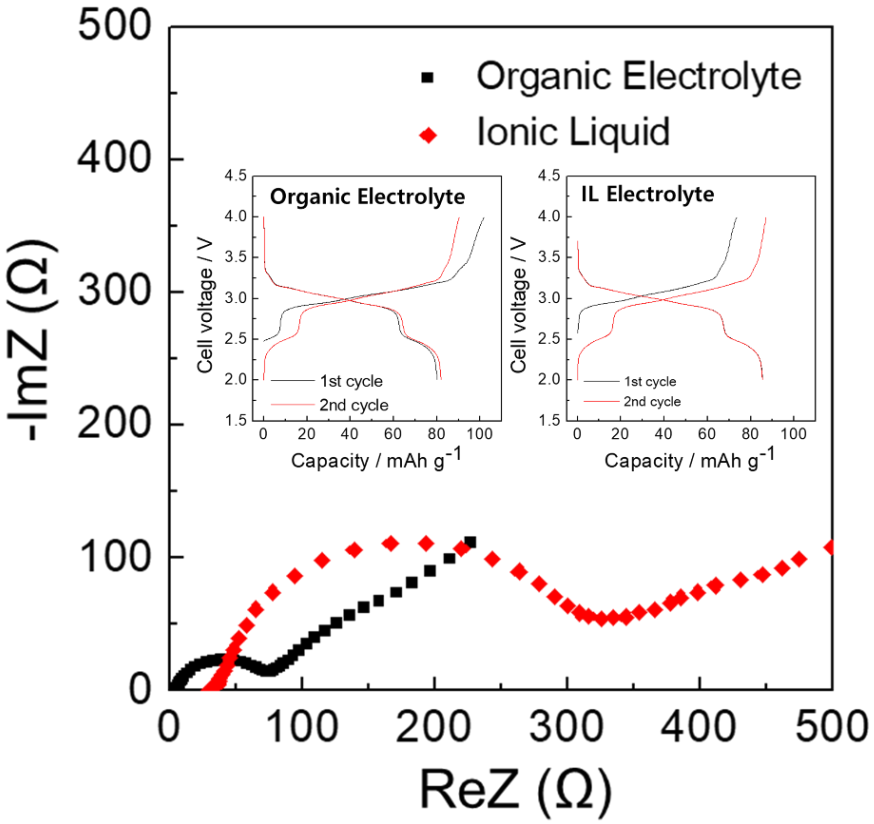

Figure 1. Nyquist plots of the Na/IL_{FSA}(x(Na[FSA])=0.3)/$Na_2FeP_2O_7$ and Na/Org/$Na_2FeP_2O_7$ half-cell (Inset: charge-discharge curves of $Na_2FeP_2O_7$ during the first two cycles at 0.1 C using the organic and IL electrolytes). Electrolytes: Na[FSA]-[C_2C_1im][FSA] (x(Na[FSA] = 0.3) and 1 M $NaClO_4$/PC, temperature: 298 K, SOC = 50%, frequency range: 10 mHz – 100 kHz, ac perturbation: 10 mV.

Figure 1 shows the Nyquist plots of the Na/IL_{FSA}(x(Na[FSA]=0.3)/$Na_2FeP_2O_7$ and Na/Org/$Na_2FeP_2O_7$ (Org = 1 M $NaClO_4$/PC (PC: propylene carbonate)) half-cells at 298 K after they were fully charged and half-discharged (SOC = 0.5). The charge-discharge curves during the first two cycles are also shown. A semicircle is observed with characteristic frequencies of 398 Hz for Na/Org/$Na_2FeP_2O_7$ and 220 Hz for Na/IL_{FSA}(x(Na[FSA]=0.3)/$Na_2FeP_2O_7$. The semicircle observed in the Nyquist plot of the Na/IL_{FSA}(x(Na[FSA]=0.3)/$Na_2FeP_2O_7$ half-cell is significantly

larger than that of the Na/Org/$Na_2FeP_2O_7$ half-cell. This large semicircle originates from the surface film between the Na metal electrode and IL electrolyte, as shown in previous work[34], and as is also confirmed by the symmetric sodium metal cells described below.

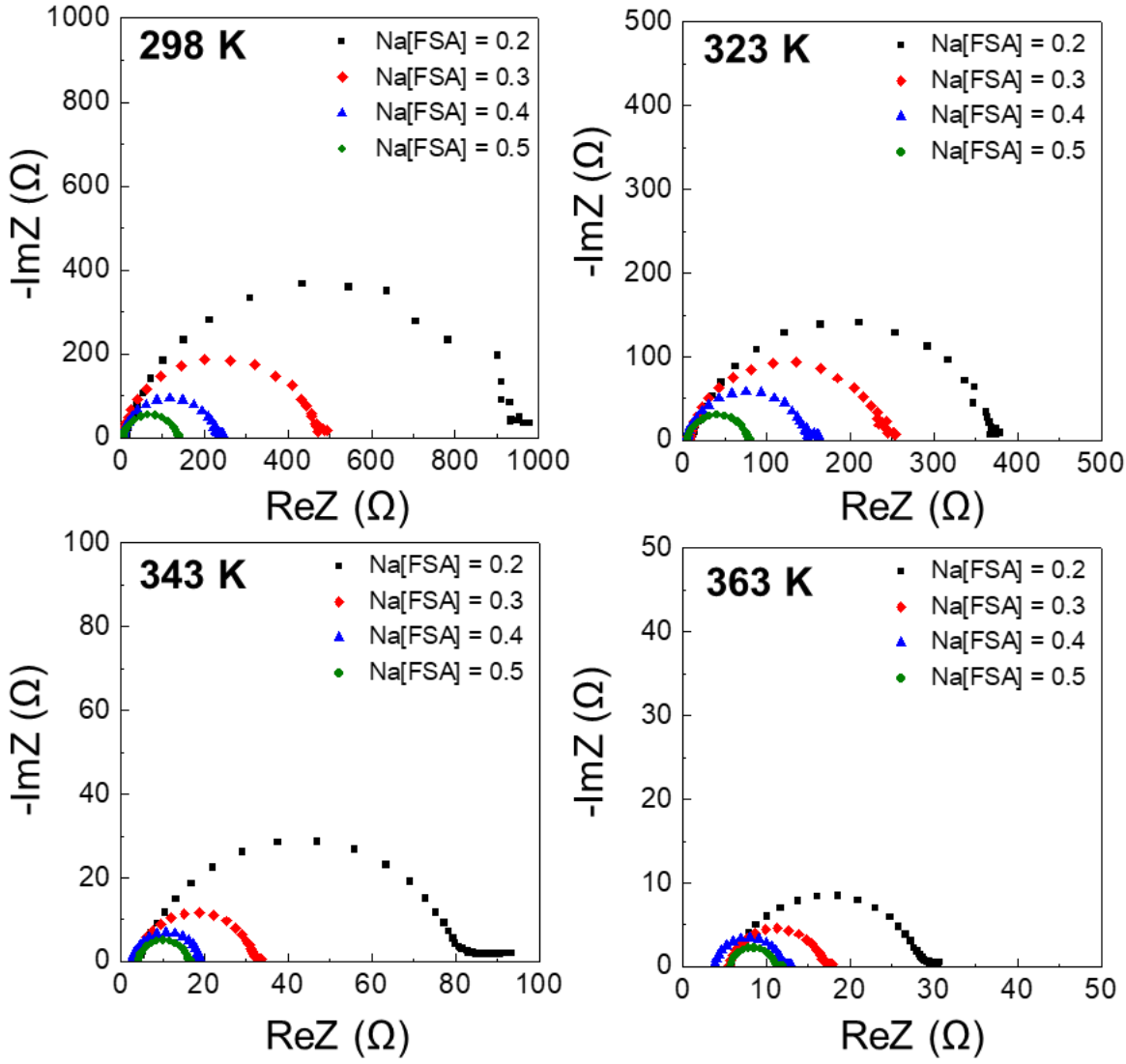

Figure 2. Nyquist plots of the Na/IL_{FSA}/Na symmetric cells in the temperature range 298–363 K. Electrolyte: Na[FSA]-[C_2C_1im][FSA] (*x*(Na[FSA]= 0.2–0.5), ac perturbation: 10 mV, frequency range: 10 mHz–100 kHz. The characteristic frequencies for the semicircles are approximately 500–150 Hz at 298 K, 1,000–350 Hz at 323 K, 5,500–1,500 Hz at 343 K, and 10,000–5,000 Hz at 363 K.

Figure 2 displays the Nyquist plots of symmetric sodium metal cells with IL_{FSA} ($Na/IL_{FSA}/Na$) at 298 K to 363 K. As mentioned above, the $Na/IL_{FSA}/Na$ cell exhibits a large semicircle. The characteristic frequency of this semicircle varies from 10,000 to 150 Hz, depending on the value of *x* in *x*(Na[FSA]) and the temperatures. Here, characteristic frequency indicates corresponding frequency at a peak of semi-circles which can help assignment of semi-circles in Nyquist plots. Although this includes a contribution from the surface film observed at high frequencies,[34] the charge-transfer resistance may also play a role, and thus the semicircle may actually consist of two semicircles. The contribution of the surface film is considered to be larger at high temperatures and high *x*(Na[FSA]) because the characteristic frequency increases with increasing temperature and *x*(Na[FSA]) in Figure 2. The EIS of the $Na/IL_{FSA}/Na$ cell has a dependency on temperature and *x*(Na[FSA]); the semicircle becomes small as the temperature and *x*(Na[FSA]) in IL_{FSA} increase. In any case, however, this resistance is significantly large and prevents the accurate estimation of the target electrodes in a half-cell configuration. This is the reason why half-cell EIS is not suitable to investigate the charge-transfer mechanism of sodium secondary batteries using IL electrolytes; thus, the SCEIS measurements of the cell composed of only the target electrodes are preferable to obtain reliable impedance data.[29, 43-44]

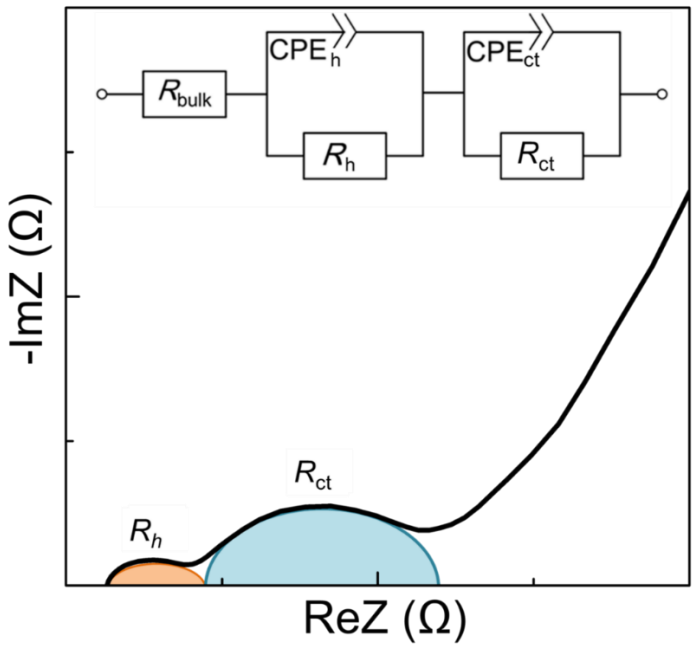

Figure 3. Schematic drawing of the Nyquist plot for a symmetric cell with two identical positive electrode materials and the equivalent circuit used for fitting the $Na_2FeP_2O_7$/Na[FSA]-[C_2C_1im][FSA]/$Na_2FeP_2O_7$ symmetric cells. Typical characteristic frequencies: 16,000−7,000 Hz for R_h and 200−1 Hz for R_{ct}. CPE denotes the constant phase element.

Figure 3 displays a schematic drawing of the Nyquist plot for a symmetric cell with two identical positive electrode materials as discussed below. The plot consists of two semicircles with different characteristic frequencies (high characteristic frequency of 16,000−7,000 Hz and low characteristic frequency of 200−1 Hz. All instances in which a characteristic frequency is not mentioned in the following discussion mean that the frequency is within these frequency ranges. The Nyquist plot was fitted by the equivalent circuit shown as the inset in Figure 3. The fitting parameters include R_{bulk}, R_h with CPE_h, and R_{ct} with CPE_{ct}. The Warburg element was omitted from the equivalent circuit because fitting this element was difficult in some cases and it also affected the accuracy of R_h and R_{ct} in this study. A detailed description of each element is provided in the subsequent paragraphs.

3.2 High-frequency Characteristics of Resistance.

Although the semicircle in the high-frequency range is often interpreted as being either the resistance of the solid-electrolyte interface (SEI) [*c.f.* it is often referred to as the cathode-electrolyte interface (CEI) in the case of a positive electrode] or that of the film (surface layer), which is formed during cycles,[26, 29-30, 43, 45-46] it is not fully understood yet and is often neglected. The semicircle is observed in the Nyquist plot of a symmetric cell (e.g., $Na_2FeP_2O_7/IL_{FSA}/Na_2FeP_2O_7$) even right after assembling the coin cells, indicates that the semicircle does not merely originate from the SEI or film resistance. Herein, the resistance is named the high-frequency resistance (i.e., R_h as defined above).

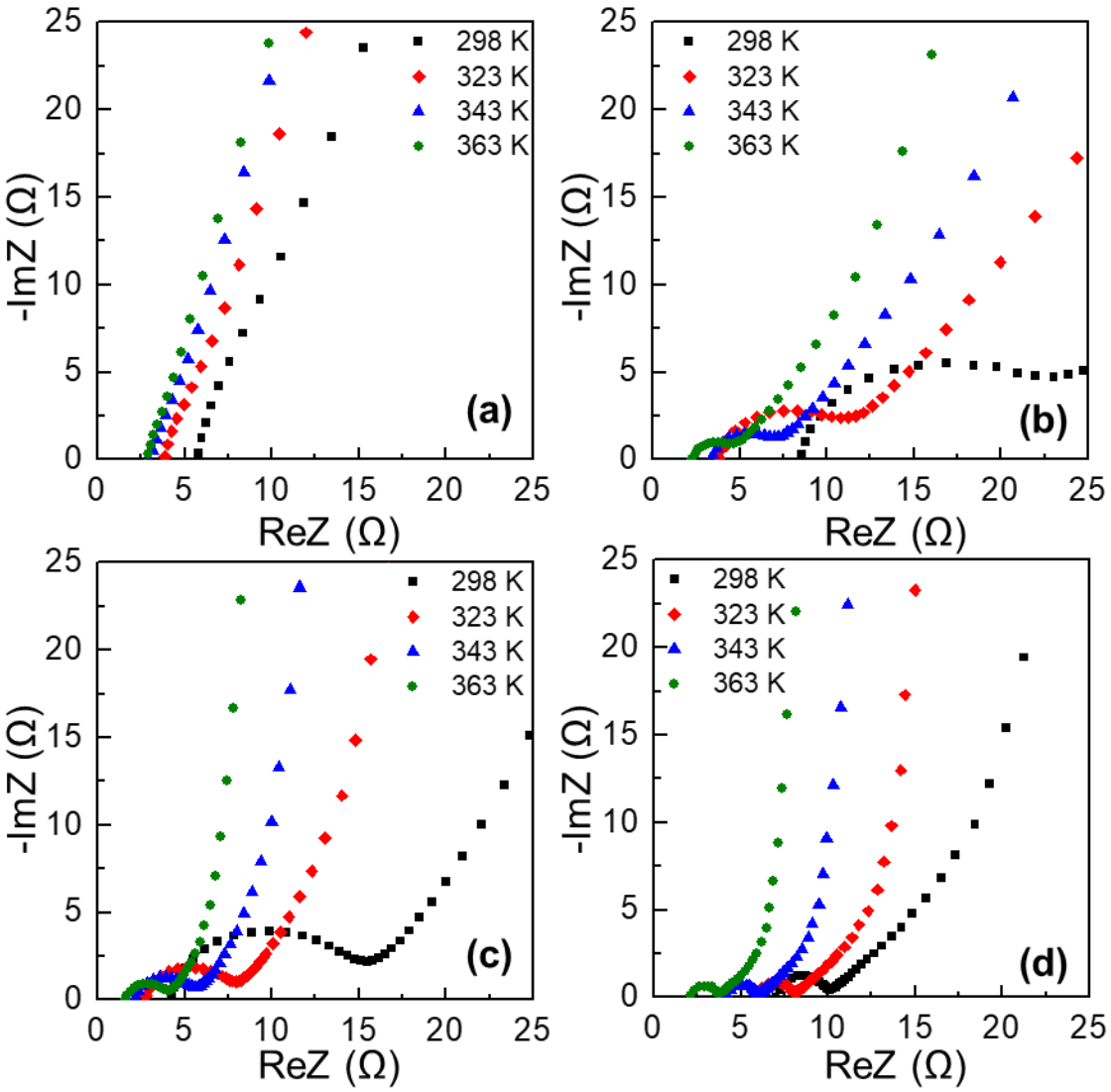

Figure 4. Nyquist plots for the AB/IL_{FSA}/AB symmetric cells in the temperature range between 298 and 363 K. (a) AB:PTFE = 5:95 wt%, (b) AB:PTFE = 50:50 wt%, (c) AB:PTFE = 95:5 wt%, and (d) pure AB pellets. Electrolyte: Na[FSA]-[C_2C_1im][FSA] (x(Na[FSA]) = 0.3), ac perturbation: 10 mV, frequency range: 100 mHz–100 kHz.

Figure 4 a–d shows the Nyquist plots of the AB/IL_{FSA}(x(Na[FSA]=0.3)/AB symmetric cell with different PTFE amounts. AB and polytetrafluoroethylene (PTFE) are a popular conductive additive and binder, respectively, for electrode fabrication. Because AB and PTFE have high and low electronic conductivities, respectively, the electronic conductivity of the entire composite electrode can be controlled by changing the ratio of AB and PTFE in the electrodes. In this

measurement, four different weight ratios of AB and PTFE were used (AB:PTFE = 5:95, 50:50, 95:5, and 100:0 (pure AB pellet) wt%). According to the Nyquist plots in Figure 4, the high-frequency region (characteristic frequency: 5,000–1,000 Hz) only contains one semicircle, which is dependent on the temperature and electronic conductivity. An increase in the temperature causes the values of R_{bulk} and R_h to decrease in all measurements. The value of R_h becomes larger as the electronic conductivity in the electrode decreases, and the electrode with 5 wt% AB exhibits very large R_h regardless of the temperature.

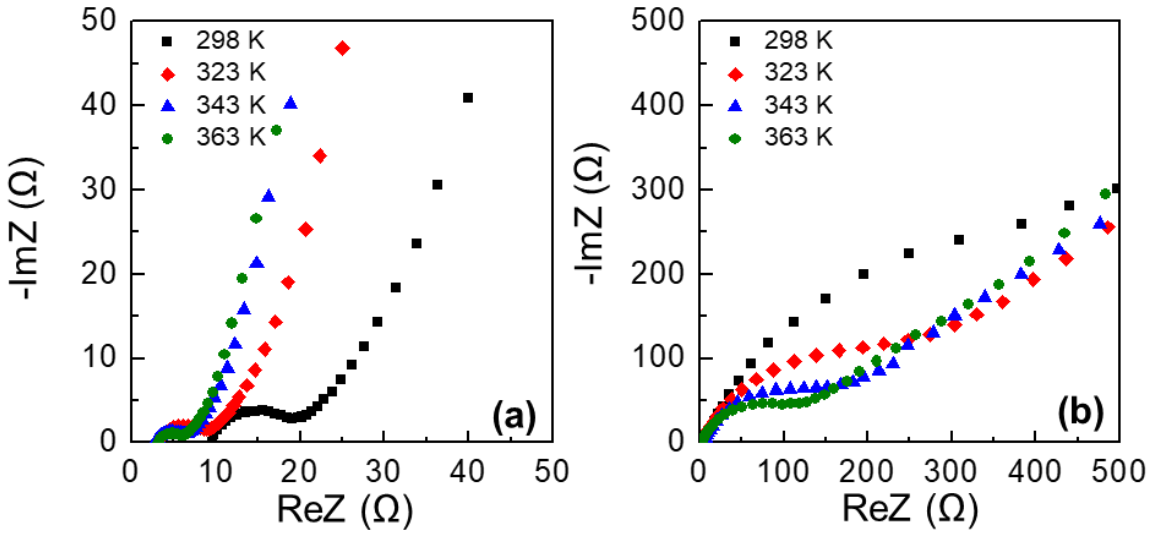

Figure 5. Nyquist plots for the V_2O_5/IL_{FSA}/V_2O_5 symmetric cells in the temperature range between 298–363 K (a) V_2O_5:AB:PTFE = 75:20:5 wt%, (b) V_2O_5:PTFE = 95:5 wt%. Electrolyte: Na[FSA]-[C_2C_1im][FSA] (x(Na[FSA] = 0.3), ac perturbation: 10 mV, frequency range: 10 mHz–100 kHz. (see Figure S6 in the Supporting Information for plots on a different scale).

Similar results were obtained using the V_2O_5 electrode (see Figure S1 and S2 Supporting Information, for SEM, EDX and XRD results of V_2O_5), which has been studied for use as positive electrode material in lithium and sodium secondary batteries.[47-51] It should be noted that the V_2O_5 electrode has a certain electronic conductivity (10^{-2}–10^{-4} S cm^{-1} at 292 K, electrical conductivity in a single crystal of V_2O_5).[52] **Figure 5a,b** shows the Nyquist plots of the V_2O_5/IL_{FSA}/V_2O_5 symmetric cell with and without AB. The V_2O_5 electrode is in a Na-free state and shows only one

semicircle in the high-frequency region corresponding to R_h because R_{ct} is too large to be observed. The semicircle of the V_2O_5 electrode without AB (Figure 5b) is significantly larger than that with AB (Figure 5a). This suggests that R_h depends on the electronic conductivity of the composite electrode because V_2O_5 has a much smaller electronic conductivity than Al metal (current collector) and AB. The SCEIS results of V_2O_5 with PVDF (PVDF = poly(vinylidene fluoride)) binder (Figure S7, Supporting Information) are similar to those in Figure 5, indicating that the EIS results are essentially independent of the binder.

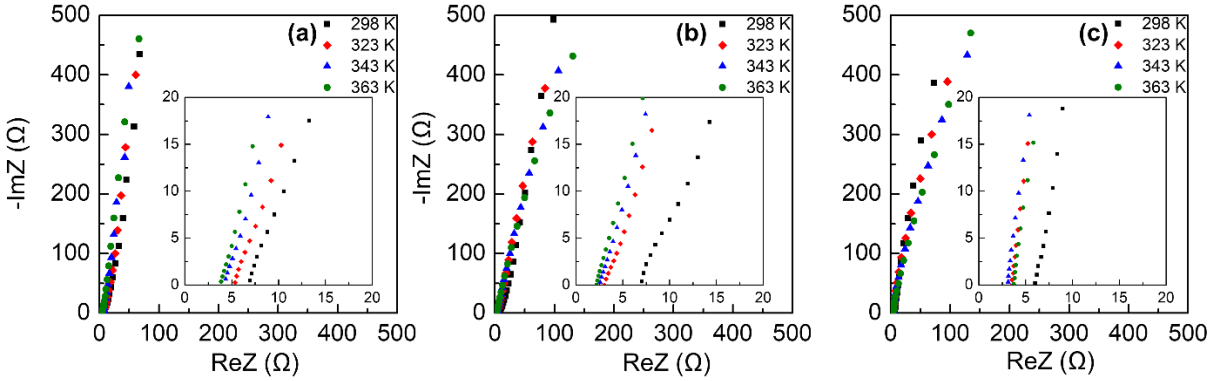

Figure 6. Nyquist plots for the (a) Al/IL_{FSA}/Al (b) Al_2O_3:PTFE/IL_{FSA}/Al_2O_3:PTFE, and (c) Al_2O_3:PVDF/IL_{FSA}/Al_2O_3:PVDF symmetric cells in the temperature range between 298–363 K (the insets show the high-frequency region). Electrolyte: Na[FSA]-[C_2C_1im][FSA] (x(Na[FSA] =0.3), ac perturbation: 10 mV, frequency range: 100 mHz–100 kHz.

Figure 6 shows the Nyquist plots of the (a) Al/IL_{FSA}/Al, (b) Al_2O_3:PTFE/IL_{FSA}/Al_2O_3:PTFE, and (c) Al_2O_3:PVDF/IL_{FSA}/Al_2O_3:PVDF symmetric cells (here Al is aluminum mesh). These data are required for a comparative study to clarify the effects of the Al current collector. Although the Nyquist plot does not show a clear semicircle, a slight curvy shape appears in the high-frequency region. The curve produced by the aluminum electrode was investigated by obtaining the EIS measurements for the α-Al_2O_3 electrode symmetric cell (α-Al_2O_3/IL_{FSA}(x(Na[FSA]=0.3)/α-Al_2O_3, where the Al_2O_3 is fixed to the Al current collector) with two different binders, PTFE and PVDF (Figure 6b,c). In the high-frequency region of the Nyquist plots, the

Al_2O_3/IL_{FSA}(x(Na[FSA]=0.3)/Al_2O_3 cell with PTFE exhibits a semicircle whereas Al_2O_3/IL_{FSA}(x(Na[FSA]=0.3)/Al_2O_3 with PVDF does not. This difference arises from the degree to which the Al surface is covered with binder; the Al current collector is not fully covered in the Al_2O_3:PTFE composite electrode whereas it is almost fully covered in the Al_2O_3:PVDF composite electrode. These results indicate that the porous insulating material (in this case there are pores among the Al_2O_3 particles) does not contribute to the semicircle in the high-frequency region and that this porous structure itself is not the origin of R_h.

Nevertheless, the value of R_h depends on x(Na[FSA]) of IL_{FSA}. The Nyquist plots for the $Na_2FeP_2O_7$ electrode symmetric cell ($Na_2FeP_2O_7$/IL_{FSA}/$Na_2FeP_2O_7$) in the high-frequency regions (see Figure 8 for the entire Nyquist plot) are shown in Figure S8 and indicate that R_h increases as x(Na[FSA]) in IL_{FSA} increases. This observation suggests that R_h is also affected by the characteristics of electrolytes.

3.3. SOC and Charge-transfer Resistance.

The semicircle in the low-frequency range is ascribed to the charge-transfer resistance, R_{ct}, which is easily influenced by the SOC of each electrode.[53-54] Considering a normal positive electrode with full cut-off voltages, R_{ct} is usually very large at SOC = 100% (or above this potential) and is reduced as SOC decreases. This is because the charge-transfer at the electrode-electrolyte interface is accelerated as SOC decreases. For particular SOCs (or a certain SOC) for which small R_{ct} values are observed, R_{ct} reaches a large value at the end of the discharge curve. (For commercial secondary batteries, SOC = 100% is not defined as the fully desodiated (delithiated) state. Here, we define SOC = 100% as meaning the Na-free state (i.e., the fully desodiated state), and SOC = 0% as the fully sodiated state.)

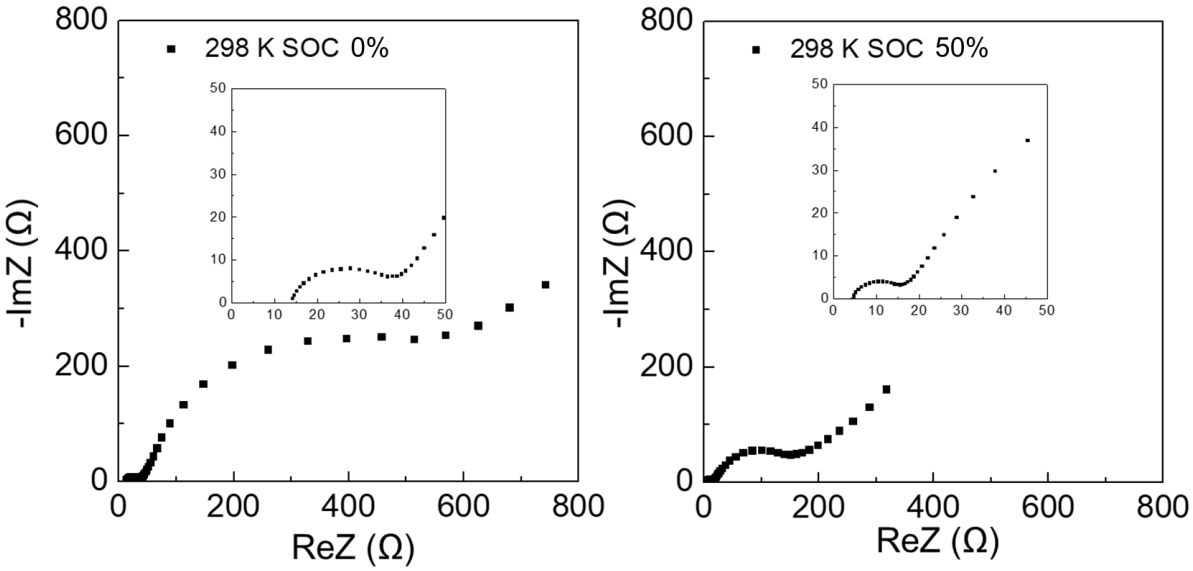

Figure 7. Comparative Nyquist plots of the $Na_2FeP_2O_7$/IL_{FSA}(x(Na[FSA]=0.3)/$Na_2FeP_2O_7$ symmetric cells at 298 K at (a) SOC = 0% and (b) SOC = 50%. The insets show the magnified plots at high frequencies. Electrolyte: Na[FSA]-[C_2C_1im][FSA] (x(Na[FSA] =0.3), ac perturbation: 10 mV and frequency range: 10 mHz–100 kHz.

Figure 7a,b shows the Nyquist plots of the $Na_2FeP_2O_7$/Na[FSA]-[C_2C_1im][FSA]/$Na_2FeP_2O_7$ symmetric cells at SOC = 0 and 50 %. The size of the semicircles for R_h and R_{ct} is highly dependent on the SOC and dramatically decreases when the SOC changes from 0 to 50%. Although this dependency of the resistance on the SOC is expected from the charge-discharge curves in Figure 1, the large R_h at SOC = 0% compared to that at SOC = 50 % suggests that R_h is also related to the SOC of electrode materials. **Table 1** summarizes the characteristics of R_h as observed by SCEIS. These results suggest that R_h cannot be explained by a single factor such as the surface film, resistance between the current collector and electrode materials, and SEI cycles,[26, 29-30, 43, 45-46] and appears on the EIS as a combination of these complicated factors.

Table 1 Summary of parameters affecting the semicircle in the high-frequency region

Parameters	Condition	State of semicircle
Temperature	Increase	Size decrease
Amount of AB	Increase	Size decrease
Electrical conductivity of the composite electrode	Increase	Size decrease
Surface area	Increase	Size decrease
Al mesh	Without active material	Small but observed
α-Al_2O_3 on Al mesh with PTFE binder	Partially covered	Small but observed
α- Al_2O_3 on Al mesh with PVDF binder	Almost fully covered	Not observed
x(Na[FSA]) in electrolyte	Increase	Size increase
Electrode SOC	Change[a]	Change[a]

[a]Contribution of SOC is complicated: refer to the text.

3.4. Activation Energy of R_{ct} and R_h in $Na_2FeP_2O_7$/IL_{FSA}/$Na_2FeP_2O_7$ symmetric cells.

As mentioned in the Introduction, the rate capability of $Na_2FeP_2O_7$ is considerably improved by intermediate-temperature operation using the Na[FSA]-[C_2C_1im][FSA] and Na[FSA]-[C_3C_1pyrr][FSA] IL electrolytes.[19,39, 42] The activation energies of R_{ct} and R_h are discussed below in an attempt to develop an improved understanding of this phenomenon.

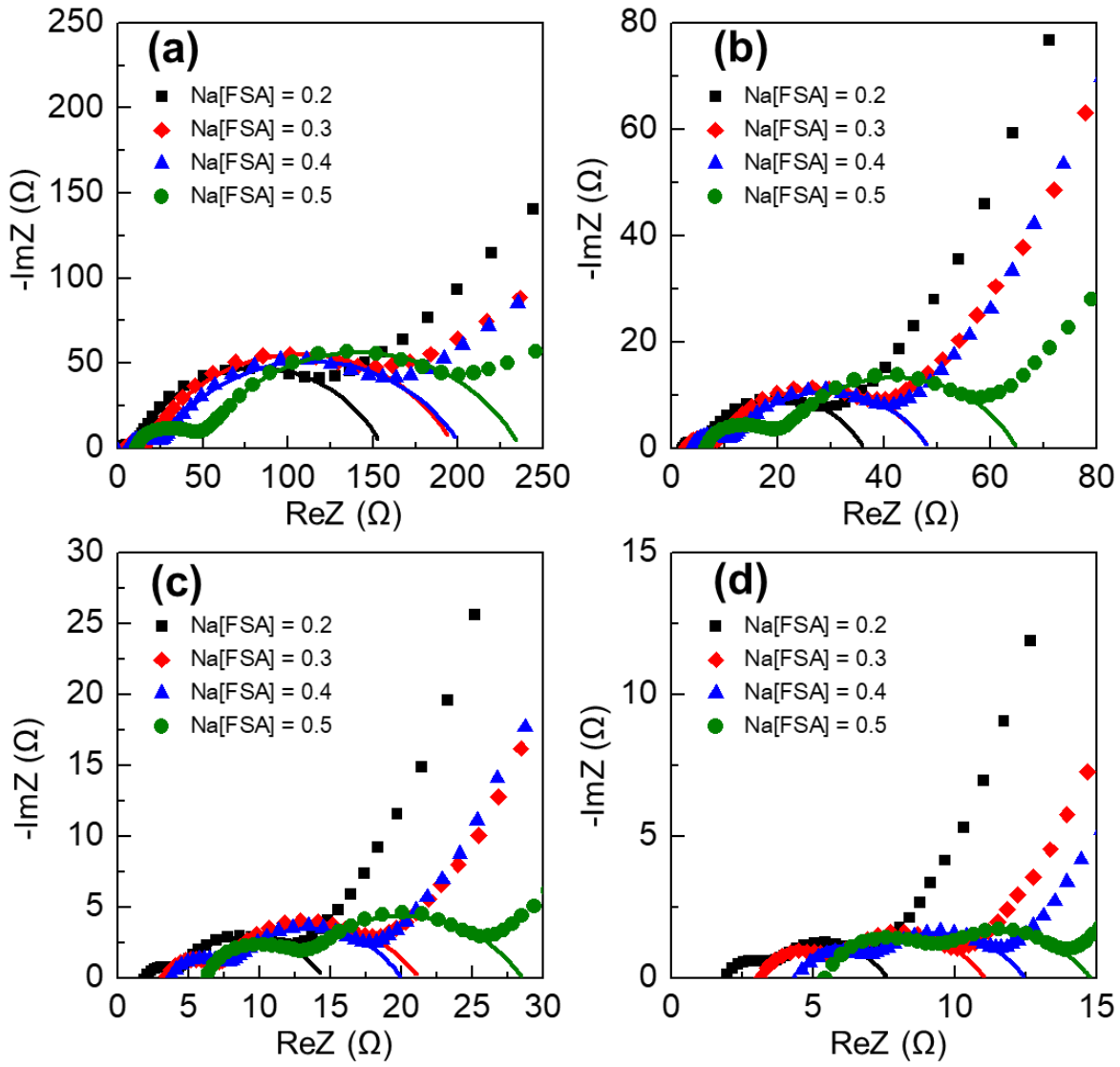

Figure 8. Nyquist plots and EIS fitting for the $Na_2FeP_2O_7$/IL_{FSA}/$Na_2FeP_2O_7$ symmetric cells at (a) 298 K, (b) 323 K, (c) 343 K, and (d) 363 K. Electrolyte: Na[FSA]-[C_2C_1im][FSA] (*x*(Na[FSA] = 0.2–0.5), SOC = 50 %, ac perturbation: 10 mV, frequency range: 10 mHz–100 kHz (see Figure S6, Supporting Information, for plots at a different scale and see Figure 2 for the equivalent circuit, and Table S1 for the EIS fitted parameters).

Figure 8a–d shows the Nyquist plots and EIS fitting of the $Na_2FeP_2O_7$/IL_{FSA}/$Na_2FeP_2O_7$ symmetric cells for different values of *x*(Na[FSA]) and temperatures (see Figure 3 for the equivalent circuit used and Table S1 for the fitting parameters). Figure S8 provides the magnified Nyquist plots for the $Na_2FeP_2O_7$/IL_{FSA}/$Na_2FeP_2O_7$ symmetric cells in Figure 8 for improved

visualization of R_h. Although both R_{ct} and R_h tend to decrease as the temperature increases and x(Na[FSA]) decreases, R_{ct} exhibits higher temperature dependency than R_h, leading to the relatively lower contribution of R_{ct} to the electrode kinetics at elevated temperatures.

The Arrhenius plot and activation energy derived from it provide a more quantitative measure for the kinetics of the electrochemical reaction for different values of x(Na[FSA]) in IL_{FSA}.[55-58] The activation energies of R_{ct} can be calculated by the following equation:[55-56]

$$ln(\frac{1}{R}) = -\left(\frac{E_a}{R_g}\right)\left(\frac{1}{T}\right) + \mathrm{In}(A),$$

where R, R_g, A, and T denote the resistance (R_{ct} or R_h), gas constant, frequency factor, and absolute temperature, respectively. The activation energy, E_a, corresponds to the slope of the linear fitting line multiplied by R_g for each plot.

Figure 9 shows the Arrhenius plots of R_h^{-1} and R_{ct}^{-1}. **Table 2** provides the calculated activation energies for R_h^{-1} and R_{ct}^{-1}. The E_a value for R_h^{-1} is 24.9 kJ mol^{-1} at x(Na[FSA]) = 0.2 and increases as the Na[FSA] fraction increases to 36.1 kJ mol^{-1} at x(Na[FSA]) = 0.5. On the other hand, E_a for R_{ct}^{-1} decreases slightly as the Na[FSA] fraction increases in IL_{FSA}, and the values of E_{ct} are 47.3 kJ mol^{-1} and 45.3 kJ mol^{-1} for x(Na[FSA]) = 0.2 and 0.5, respectively. Although the frequency factor of R_h^{-1} is larger than that of R_{ct}^{-1}, E_a for R_h^{-1} is smaller than that of R_{ct}^{-1}. Consequently, the contribution of R_h to the rate capability becomes more significant as the temperature increases from 298 K to 363 K. Contrary to this, the contribution of R_{ct} shows the reverse trend in that it is more significant at 298 K than at 363 K. These results indicate that the rate capability is highly dependent on R_{ct} at room temperature, at which R_{bulk} and R_h are relatively minor factors. As the temperature increases, R_{ct} rapidly decreases, and all three of these factors (R_{bulk}, R_h, and R_{ct}) affect the polarization of the $Na_2FeP_2O_7$ electrode at intermediate temperatures.

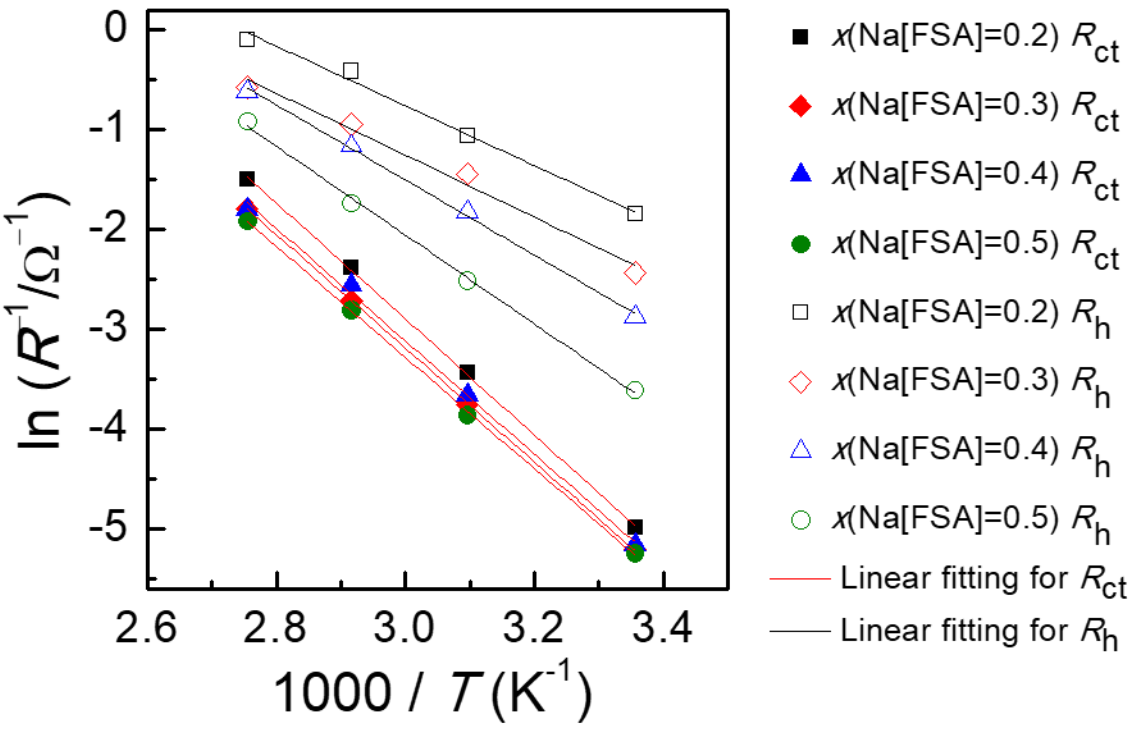

Figure 9. Arrhenius plots of R_h^{-1} and R_{ct}^{-1} using the EIS fitted parameters of the $Na_2FeP_2O_7$/IL_{FSA}/$Na_2FeP_2O_7$ symmetric cell.

Table 2. Activation energy obtained from Arrhenius plots based on the EIS fitting parameters for the $Na_2FeP_2O_7$/IL_{FSA}/$Na_2FeP_2O_7$ symmetric cells (see EIS fitted plots in Figure 8, EIS parameters in Table S1, and Arrhenius plots in Figure 9).

x(Na[FSA]) / %	E_a for R_h / kJ mol^{-1}	E_a for R_{ct} / kJ mol^{-1}
0.2	24.9	47.3
0.3	25.6	46.4
0.4	30.6	46.0
0.5	36.1	45.3

4. CONCLUSIONS

We used SCEIS to examine positive electrode materials for sodium secondary batteries using ILs with the aim of clarifying the factors that contribute to battery performance. In this regard, the use of SCEIS as a measurement technique provides a convenient, fast, and non-destructive

method that enables the following information on R_h and R_{ct} to be obtained. By changing the parameters related to EIS, R_h was found to appear as a combination of the effects of temperature, Na[FSA] fraction, electronic conductivity of the composite electrode, ionic conductivity of the electrolyte, and SOC. The activation energies of R_h and R_{ct}, which were obtained by linear fitting of the Arrhenius plots, provided a clear understanding of the temperature dependence of the electrochemical performance of $Na_2FeP_2O_7$ in ILs. These results indicated that the improvement in the rate capability at elevated temperatures mainly resulted from the decrease in R_{ct}. At intermediate temperatures, R_{bulk}, R_h, and R_{ct} all make a certain contribution to the rate performance.

Although the present study focused on sodium secondary batteries with ionic liquid electrolytes, the interpretation of the results obtained here provides useful and comprehensive information for other systems including those based on other secondary batteries using organic electrolytes or those operating at different temperatures. The results of the EIS analysis presented in this paper are foreseen to facilitate the future development of new electrode and electrolyte systems.

ASSOCIATED CONTENT

Supporting Information

The Supporting Information is available free of charge on the ACS Publications website at DOI: XXXXXXX.

Electrochemical impedance spectroscopic data (Nyquist plots and fitting parameters) and analytical data (SEM, EDS and XRD) for electrode materials (PDF)

AUTHOR INFORMATION

Corresponding Author

*Phone: +81 75 753 5827. Fax: +81 75 753 5906. E-mail: k-matsumoto@energy.kyoto-u.ac.jp (K.M.).

Notes

The authors declare no competing financial interest.

ACKNOWLEDGMENT
This study was partly supported by the Advanced Low Carbon Technology Research and Development Program (ALCA) of the Japan Science and Technology Agency (JST) and the Japanese Ministry of Education, Culture, Sports, Science and Technology (MEXT) program "Elements Strategy Initiative to Form Core Research Center."

REFERENCES

(1) Ellis, B. L.; Nazar, L. F. Sodium and Sodium-ion Energy Storage Batteries. *Curr. Opin. Solid State Mater. Sci.* **2012,** *16*, 168-177.
(2) Slater, M. D.; Kim, D.; Lee, E.; Johnson, C. S. Sodium-Ion Batteries. *Adv. Funct. Mater.* **2013,** *23*, 947-958.
(3) Yabuuchi, N.; Kubota, K.; Dahbi, M.; Komaba, S. Research Development on Sodium-Ion Batteries. *Chem. Rev.* **2014,** *114*, 11636-11682.
(4) Feng, L.; Zhen, Z. Micro/Nanostructured Materials for Sodium Ion Batteries and Capacitors. *Small* **2018,** *14,* 1702961.
(5) Palacin, M. R. Recent Advances in Rechargeable Battery Materials: A Chemist's Perspective. *Chem. Soc. Rev.* **2009,** *38*, 2565-2575.
(6) Hwang, J.-Y.; Myung, S.-T.; Sun, Y.-K. Sodium-ion Batteries: Present and Future. *Chem. Soc. Rev.* **2017,** *46*, 3529-3614.
(7) Kim, S.-W.; Seo, D.-H.; Ma, X.; Ceder, G.; Kang, K. Electrode Materials for Rechargeable Sodium-Ion Batteries: Potential Alternatives to Current Lithium-Ion Batteries. *Adv. Energy Mater.* **2012,** *2*, 710-721.
(8) Barpanda, P.; Lander, L.; Nishimura, S.-i.; Yamada, A. Polyanionic Insertion Materials for Sodium-Ion Batteries. *Adv. Energy Mater.* **2018,** *8*, 1703055.
(9) Kim, D.; Lee, E.; Slater, M.; Lu, W.; Rood, S.; Johnson, C. S. Layered $Na[Ni_{1/3}Fe_{1/3}Mn_{1/3}]O_2$ Cathodes for Na-ion Battery Application. *Electrochem. Commun.* **2012,** *18*, 66-69.
(10) Armand, M.; Endres, F.; MacFarlane, D. R.; Ohno, H.; Scrosati, B. Ionic-liquid Materials for the Electrochemical Challenges of the Future. *Nat. Mater.* **2009,** *8*, 621.
(11) Lewandowski, A.; Świderska-Mocek, A. Ionic Liquids as Electrolytes for Li-ion Batteries—An Overview of Electrochemical Studies. *J. Power Sources* **2009,** *194*, 601-609.
(12) Hosokawa, T.; Matsumoto, K.; Nohira, T.; Hagiwara, R.; Fukunaga, A.; Sakai, S.; Nitta, K. Stability of Ionic Liquids against Sodium Metal: A Comparative Study of 1-Ethyl-3-methylimidazolium Ionic Liquids with Bis(fluorosulfonyl)amide and

Bis(trifluoromethylsulfonyl)amide. *J. Phys. Chem. C* **2016,** *120*, 9628-9636.
(13) Mohd Noor, S. A.; Howlett, P. C.; MacFarlane, D. R.; Forsyth, M. Properties of Sodium-based Ionic Liquid Electrolytes for Sodium Secondary Battery Applications. *Electrochim. Acta* **2013,** *114*, 766-771.
(14) Monti, D.; Jónsson, E.; Palacín, M. R.; Johansson, P. Ionic Liquid Based Electrolytes for Sodium-ion Batteries: Na^+ Solvation and Ionic Conductivity. *J. Power Sources* **2014,** *245*, 630-636.
(15) Appetecchi, G. B.; Montanino, M.; Passerini, S. Ionic Liquid-Based Electrolytes for High Energy, Safer Lithium Batteries. In *Ionic Liquids: Science and Applications*; American Chemical Society: 2012; Chapter 4, pp 67-128.
(16) Basile, A.; Hilder, M.; Makhlooghiazad, F.; Pozo-Gonzalo, C.; MacFarlane, D. R.; Howlett, P. C.; Forsyth, M. Ionic Liquids and Organic Ionic Plastic Crystals: Advanced Electrolytes for Safer High Performance Sodium Energy Storage Technologies. *Adv. Energy Mater.* **2018,** *8*, 1703491.
(17)Usui, H.; Domi, Y.; Nishida, H.; Yamaguchi, K.; Yamagami, R.; Sakaguchi, H. Enhanced Performance of Sn_4P_3 Electrode Cycled in Ionic Liquid Electrolyte at Intermediate Temperature as Na-Ion Battery Anode. *ChemistrySelect* **2018,** *3*, 8462-8467.
(18) Hwang, J.; Matsumoto, K.; Orikasa, Y.; Katayama, M.; Inada, Y.; Nohira, T.; Hagiwara, R. Crystalline Maricite $NaFePO_4$ as a Positive Electrode Material for Sodium Secondary Batteries Operating at Intermediate Temperature. *J. Power Sources* **2018,** *377*, 80-86.
(19) Chen, C.-Y.; Kiko, T.; Hosokawa, T.; Matsumoto, K.; Nohira, T.; Hagiwara, R. Ionic Liquid Electrolytes with High Sodium Ion Fraction for High-rate and Long-life Sodium Secondary Batteries. *J. Power Sources* **2016,** *332*, 51-59.
(20) Yamamoto, T.; Nohira, T.; Hagiwara, R.; Fukunaga, A.; Sakai, S.; Nitta, K.; Inazawa, S. Improved Cyclability of Sn-Cu Film Electrode for Sodium Secondary Battery Using Inorganic Ionic Liquid Electrolyte. *Electrochim. Acta* **2014,** *135*, 60-67.
(21) Chen, C.-Y.; Matsumoto, K.; Nohira, T.; Hagiwara, R.; Orikasa, Y.; Uchimoto, Y. Pyrophosphate $Na_2FeP_2O_7$ as a Low-cost and High-performance Positive Electrode Material for Sodium Secondary Batteries Utilizing an Inorganic Ionic Liquid. *J. Power Sources* **2014,** *246*, 783-787.
(22) Fukunaga, A.; Nohira, T.; Hagiwara, R.; Numata, K.; Itani, E.; Sakai, S.; Nitta, K.; Inazawa, S. A Safe and High-rate Negative Electrode for Sodium-ion Batteries: Hard Carbon in NaFSA-C_1C_3pyrFSA Ionic Liquid at 363 K. *J. Power Sources* **2014,** *246*, 387-391.
(23) Hwang, J.; Matsumoto, K.; Nohira, T.; Hagiwara, R. Electrochemical Sodiation-desodiation of Maricite $NaFePO_4$ in Ionic Liquid Electrolyte. *Electrochemistry* **2017,** *85*, 675-679.
(24) Hwang, J.; Matsumoto, K.; Hagiwara, R. $Na_3V_2(PO_4)_3$/C Positive Electrodes with High Energy and Power Densities for Sodium Secondary Batteries with Ionic Liquid Electrolytes That Operate across Wide Temperature Ranges. *Adv. Sustainable Syst.* **2018,** *2*, 1700171.
(25) Kaushik, S.; Hwang, J.; Matsumoto, K.; Sato Y.; Hagiwara, R. CuP_2/C Composite Negative Electrodes for Sodium Secondary Batteries Operating at Room-to-Intermediate Temperatures Utilizing Ionic Liquid Electrolyte. *ChemElectroChem* **2018,** *5*, 1340-1344.
(26) Andre, D.; Meiler, M.; Steiner, K.; Wimmer, C.; Soczka-Guth, T.; Sauer, D. U. Characterization of High-power Lithium-ion Batteries by Electrochemical Impedance Spectroscopy. I. Experimental Investigation. *J. Power Sources* **2011,** *196*, 5334-5341.
(27) Chang, B.-Y.; Park, S.-M. Electrochemical Impedance Spectroscopy. *Annu Rev. of Anal. Chem.* **2010,** *3*, 207-229.

(28) Guo, J.; Sun, A.; Chen, X.; Wang, C.; Manivannan, A. Cyclability Study of Silicon–carbon Composite Anodes for Lithium-ion Batteries Using Electrochemical Impedance Spectroscopy. *Electrochim. Acta* **2011,** *56*, 3981-3987.
(29) Wohde, F.; Balabajew, M.; Roling, B. Li^+Transference Numbers in Liquid Electrolytes Obtained by Very-Low-Frequency Impedance Spectroscopy at Variable Electrode Distances. *J. Electrochem. Soc.* **2016,** *163*, A714-A721.
(30) Lu, P.; Li, C.; Schneider, E. W.; Harris, S. J. Chemistry, Impedance, and Morphology Evolution in Solid Electrolyte Interphase Films during Formation in Lithium Ion Batteries. *J. Phys. Chem. C* **2014,** *118*, 896-903.
(31) Park, S.-M.; Yoo, J.-S. Peer Reviewed: Electrochemical Impedance Spectroscopy for Better Electrochemical Measurements. *Anal. Chem.* **2003,** *75*, 455 A-461 A.
(32) Thomas, M. G. S. R.; Bruce, P. G.; Goodenough, J. B. AC Impedance Analysis of Polycrystalline Insertion Electrodes: Application to $Li_{1-x}CoO_2$. *J. Electrochem. Soc.* **1985,** *132*, 1521-1528.
(33) Woo, S.-U.; Park, B.-C.; Yoon, C. S.; Myung, S.-T.; Prakash, J.; Sun, Y.-K. Improvement of Electrochemical Performances of $Li[Ni_{0.8}Co_{0.1}Mn_{0.1}]O_2$ Cathode Materials by Fluorine Substitution. *J. Electrochem. Soc.* **2007,** *154*, A649-A655.
(34) Matsumoto, K.; Hosokawa, T.; Nohira, T.; Hagiwara, R.; Fukunaga, A.; Numata, K.; Itani, E.; Sakai, S.; Nitta, K.; Inazawa, S. The Na[FSA-[C_2C_1im][FSA] ($C_2C_1im^+$:1-ethyl-3-methylimidazolium and FSA^-:bis(fluorosulfonyl)amide) Ionic Liquid Electrolytes for Sodium Secondary Batteries. *J. Power Sources* **2014**, 265, 36-39.
(35) Wang, C.-H.; Yang, C.-H.; Chang, J.-K. Suitability of Ionic Liquid Electrolytes for Room-temperature Sodium-ion Battery Applications. *Chem. Commun.* **2016,** *52*, 10890-10893.
(36) Barpanda, P.; Ye, T.; Nishimura, S.-i.; Chung, S.-C.; Yamada, Y.; Okubo, M.; Zhou, H.; Yamada, A. Sodium Iron Pyrophosphate: A Novel 3.0V Iron-based Cathode for Sodium-ion Batteries. *Electrochem. Commun.* **2012,** *24*, 116-119.
(37) Barpanda, P.; Liu, G.; Ling, C. D.; Tamaru, M.; Avdeev, M.; Chung, S.-C.; Yamada, Y.; Yamada, A. $Na_2FeP_2O_7$: A Safe Cathode for Rechargeable Sodium-ion Batteries. *Chem. Mater.* **2013,** *25*, 3480-3487.
(38) Kim, H.; Shakoor, R. A.; Park, C.; Lim, S. Y.; Kim, J.-S.; Jo, Y. N.; Cho, W.; Miyasaka, K.; Kahraman, R.; Jung, Y. et al. $Na_2FeP_2O_7$ as a Promising Iron-Based Pyrophosphate Cathode for Sodium Rechargeable Batteries: A Combined Experimental and Theoretical Study. *Adv. Funct. Mater.* **2013,** *23*, 1147-1155.
(39) Chen, C. Y.; Matsumoto, K.; Nohira, T.; Hagiwara, R.; Orikasa, Y.; Uchimoto, Y. Pyrophosphate $Na_2FeP_2O_7$ as a Low-cost and High-performance Positive Electrode Material for Sodium Secondary Batteries Utilizing an Inorganic Ionic Liquid. *J. Power Sources* **2014,** *246*, 783-787.
(40) Zheng, J.-c.; Yang, B.-y.; Wang, X.-w.; Zhang, B.; Tong, H.; Yu, W.-j.; Zhang, J.-f. Comparative Investigation of $Na_2FeP_2O_7$ Sodium Insertion Material Synthesized by Using Different Sodium Sources. *ACS Sustain. Chem. Eng.* **2018,** *6*, 4966-4972.
(41) Honma, T.; Togashi, T.; Ito, N.; Komatsu, T. Fabrication of $Na_2FeP_2O_7$ glass-ceramics for Sodium Ion Battery. *J. Cer. Soc. Japan*, **2012**, 120, 344-346.
(42) Chen, C.-Y.; Matsumoto, K.; Nohira, T.; Ding, C.; Yamamoto, T.; Hagiwara, R. Charge–discharge Behavior of A $Na_2FeP_2O_7$ Positive Electrode in An Ionic Liquid Electrolyte between 253 and 363 K. *Electrochim. Acta* **2014,** *133*, 583-588.
(43) Chen, C. H.; Liu, J.; Amine, K. Symmetric Cell Approach and Impedance Spectroscopy of

High Power Lithium-Ion Batteries. *J. Power Sources* **2001,** *96*, 321-328.
(44) Ogihara, N.; Kawauchi, S.; Okuda, C.; Itou, Y.; Takeuchi, Y.; Ukyo, Y. Theoretical and Experimental Analysis of Porous Electrodes for Lithium-Ion Batteries by Electrochemical Impedance Spectroscopy Using a Symmetric Cell. *J. Electrochem. Soc.* **2012,** *159*, A1034-A1039.
(45) Alcántara, R.; Jaraba, M.; Lavela, P.; Tirado, J. L. X-ray Diffraction and Electrochemical Impedance Spectroscopy Study of Zinc Coated $LiNi_{0.5}Mn_{1.5}O_4$ Electrodes. *J. Electroanal. Chem.* **2004,** *566*, 187-192.
(46) Croce, F.; Nobili, F.; Deptula, A.; Lada, W.; Tossici, R.; D'Epifanio, A.; Scrosati, B.; Marassi, R. An Electrochemical Impedance Spectroscopic Study of the Transport Properties of $LiNi0._{75}Co_{0.25}O_2$. *Electrochem. Commun.* **1999,** *1*, 605-608.
(47) Raju, V.; Rains, J.; Gates, C.; Luo, W.; Wang, X.; Stickle, W. F.; Stucky, G. D.; Ji, X. Superior Cathode of Sodium-Ion Batteries: Orthorhombic V_2O_5 Nanoparticles Generated in Nanoporous Carbon by Ambient Hydrolysis Deposition. *Nano Lett.* **2014,** *14*, 4119-4124.
(48) Cao, A.-M.; Hu, J.-S.; Liang, H.-P.; Wan, L.-J. Self-Assembled Vanadium Pentoxide (V_2O_5) Hollow Microspheres from Nanorods and Their Application in Lithium-Ion Batteries. *Angew. Chem. Int. Ed.* **2005,** *44* , 4391-4395.
(49) Li, H.-Y.; Yang, C.-H.; Tseng, C.-M.; Lee, S.-W.; Yang, C.-C.; Wu, T.-Y.; Chang, J.-K. Electrochemically Grown Nanocrystalline V_2O_5 as High-Performance Cathode for Sodium-Ion Batteries. *J. Power Sources* **2015,** *285*, 418-424.
(50) Shao, J.; Li, X.; Wan, Z.; Zhang, L.; Ding, Y.; Zhang, L.; Qu, Q.; Zheng, H. Low-Cost Synthesis of Hierarchical V_2O_5 Microspheres as High-Performance Cathode for Lithium-Ion Batteries. *ACS Appl. Mater. Interfacess* **2013,** *5*, 7671-7675.
(51) Li, X.; Liu, C.; Zhang, C.; Fu, H.; Nan, X.; Ma, W.; Li, Z.; Wang, K.; Wu, H.; Cao, G. Effects of Preinserted Na Ions on Li-Ion Electrochemical Intercalation Properties of V_2O_5. *ACS Appl. Mater. Interfacess* **2016,** *8*, 24629-24637.
(52) Bullot, J.; Gallais, O.; Gauthier, M.; Livage, J. Semiconducting Properties of Amorphous V_2O_5 Layers Deposited from Gels. *Appl. Phys. Lett.* **1980,** *36*, 986-988.
(53) Fleischer, C.; Waag, W.; Heyn, H.-M.; Sauer, D. U. On-Line Adaptive Battery Impedance Parameter and State Estimation Considering Physical Principles in Reduced Order Equivalent Circuit Battery Models: Part 1. Requirements, Critical Review of Methods and Modeling. *J. Power Sources* **2014,** *260*, 276-291.
(54) Gomez, J.; Nelson, R.; Kalu, E. E.; Weatherspoon, M. H.; Zheng, J. P. Equivalent Circuit Model Parameters of A High-Power Li-Ion Battery: Thermal and State of Charge Effects. *J. Power Sources* **2011,** *196*, 4826-4831.
(55) Abe, T.; Sagane, F.; Ohtsuka, M.; Iriyama, Y.; Ogumi, Z. Lithium-Ion Transfer at the Interface Between Lithium-Ion Conductive Ceramic Electrolyte and Liquid Electrolyte-A Key to Enhancing the Rate Capability of Lithium-Ion Batteries. *J. Electrochem. Soc.* **2005,** *152*, A2151-A2154.
(56) Sagane, F.; Abe, T.; Iriyama, Y.; Ogumi, Z. Li^+ and Na^+ Transfer through Interfaces between Inorganic Solid Electrolytes and Polymer or Liquid Electrolytes. *J. Power Sources* **2005,** *146*, 749-752.
(57) Ma, H.; Zhang, S.; Ji, W.; Tao, Z.; Chen, J. α-CuV_2O_6 Nanowires: Hydrothermal Synthesis and Primary Lithium Battery Application. *J. Am. Chem. Soc.* **2008,** *130*, 5361-5367.
(58) Gao, H.; Hu, Z.; Zhang, K.; Cheng, F.; Chen, J. Intergrown $Li_2FeSiO_4 \cdot LiFePO_4$-C Nanocomposites as High-capacity Cathode Materials for Lithium-ion Batteries. *Chem. Commun.* **2013,** *49*, 3040-3042.

TOC Graphic

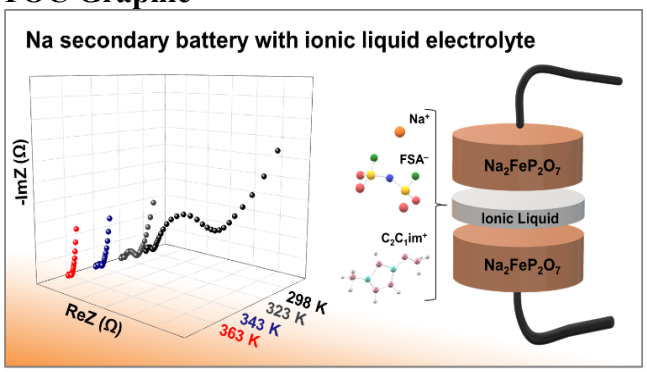
Na secondary battery with ionic liquid electrolyte
-ImZ (Ω)
ReZ (Ω)
298 K
323 K
343 K
363 K
Na+
FSA−
C2C1im+
Na2FeP2O7
Ionic Liquid
Na2FeP2O7

Supporting Information

Symmetric Cell Electrochemical Impedance Spectroscopy of $Na_2FeP_2O_7$ Positive Electrode Material in Ionic Liquid Electrolytes

Jinkwang Hwang,[†] Kazuhiko Matsumoto,[*,†,‡] and Rika Hagiwara[†,‡]
[†]*Graduate School of Energy Science, Kyoto University, Yoshida-honmachi, Sakyo-ku, Kyoto 606-8501, Japan*
[‡]*Unit of Elements Strategy Initiative for Catalysts & Batteries (ESICB), Kyoto University, Katsura, Kyoto 615-8510, Japan*

*Corresponding author: Kazuhiko Matsumoto
E-mail: k-matsumoto@energy.kyoto-u.ac.jp
Tel: +81757534817
Fax: +81757535906

Table S1. EIS fitting parameters, R_{bulk}, R_h, R_{ct}, Q_h, *and* Q_{ct}.

Na[FSA] / %	T /K	Resistance / Ω			CPE / F cm^2 s$^{(a-1)}$			
		R_{bulk}	R_h	R_{ct}	Q_h	a	Q_{ct}	a
0.2	298	2.91	6.34	146.0	3.80x10^{-5}	0.73	1.67x10^{-3}	0.73
	323	2.39	2.87	30.97	1.31x10^{-5}	0.87	2.43x10^{-3}	0.68
	343	2.18	1.52	10.84	4.58x10^{-6}	0.99	3.50x10^{-3}	0.63
	363	2.04	1.09	4.48	6.47x10^{-6}	0.99	3.47x10^{-3}	0.62
0.3	298	4.56	11.41	182.0	1.34x10^{-5}	0.79	4.43x10^{-3}	0.69
	323	2.98	4.24	42.95	1.80x10^{-6}	0.99	2.58x10^{-3}	0.61
	343	3.65	2.58	15.02	2.71x10^{-6}	0.99	2.94x10^{-3}	0.60
	363	3.32	1.78	5.96	3.70x10^{-6}	0.99	2.89x10^{-3}	0.61
0.4	298	6.12	17.66	174.4	1.54x10^{-5}	0.75	1.43x10^{-3}	0.68
	323	3.82	6.198	38.53	6.84x10^{-6}	0.87	2.16x10^{-3}	0.64
	343	3.95	3.20	13.85	7.31x10^{-6}	0.90	2.54x10^{-3}	0.63
	363	4.61	1.80	6.06	3.81x10^{-6}	0.99	1.80x10^{-3}	0.61
0.5	298	10.43	36.89	189.5	1.86x10^{-5}	0.71	1.09x10^{-3}	0.51
	323	6.49	12.33	47.16	1.28x10^{-5}	0.79	1.58x10^{-3}	0.66
	343	6.39	5.66	16.48	7.31x10^{-6}	0.87	2.10x10^{-3}	0.62
	363	5.63	2.50	6.77	3.03x10^{-6}	0.96	2.63x10^{-3}	0.57

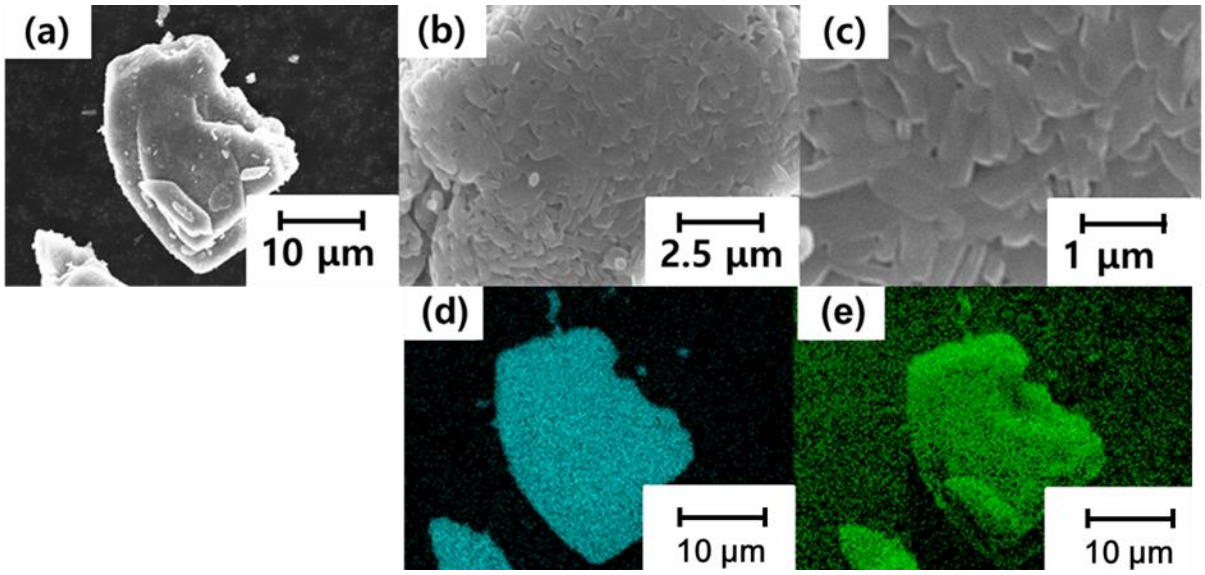

Figure S1. (a-c) SEM images at different magnifications and EDS mapping of (d) vanadium and (f) oxygen for V_2O_5 used in this study.

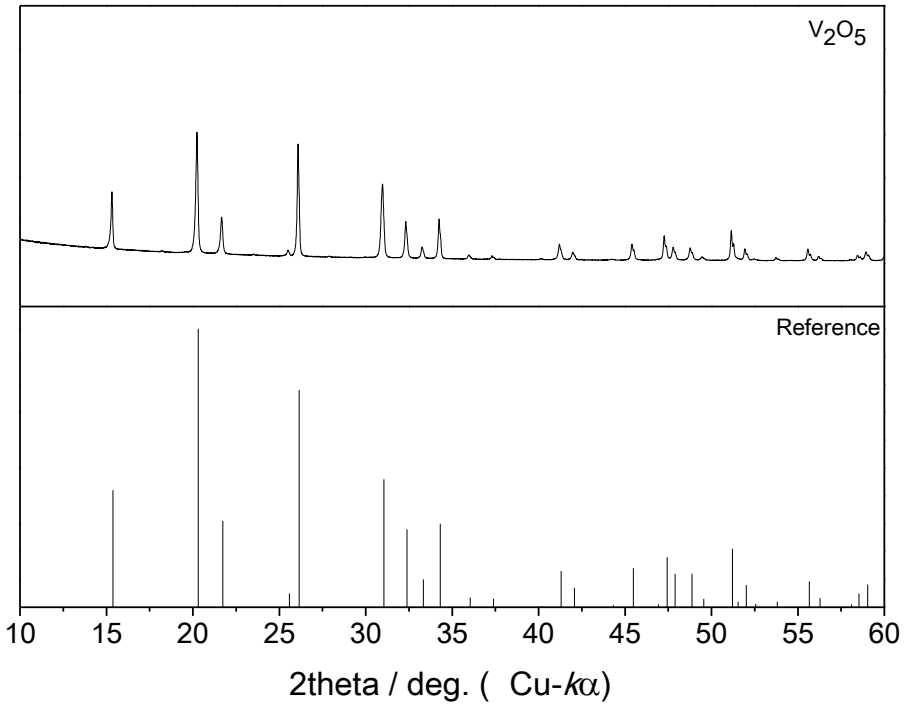

Figure S2. XRD patterns of V_2O_5.

Brief comments: The V_2O_5 is indexed as an orthorhombic crystal system with space group *Pmmn* via reference.

[Reference] R. Enjalbert, J. Galy, *Acta Crystallogr. C* **1986**, 42, 1467.

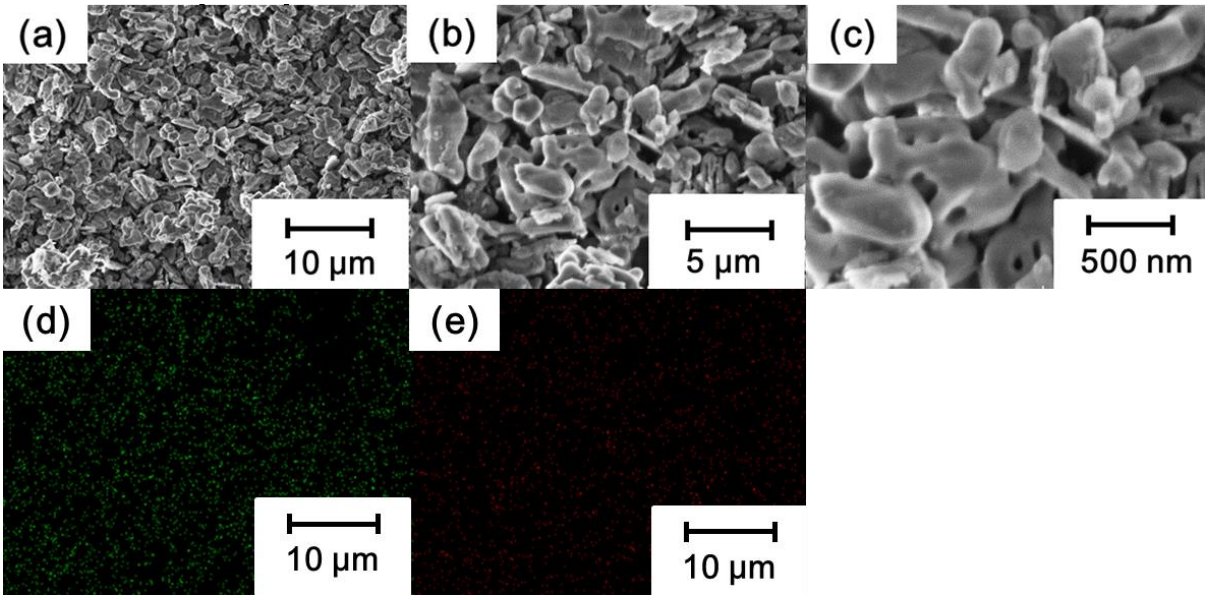

Figure S3. (a-c) SEM images at different magnifications and EDS mapping of (d) oxygen and (f) aluminum for α-Al_2O_3 used in this study.

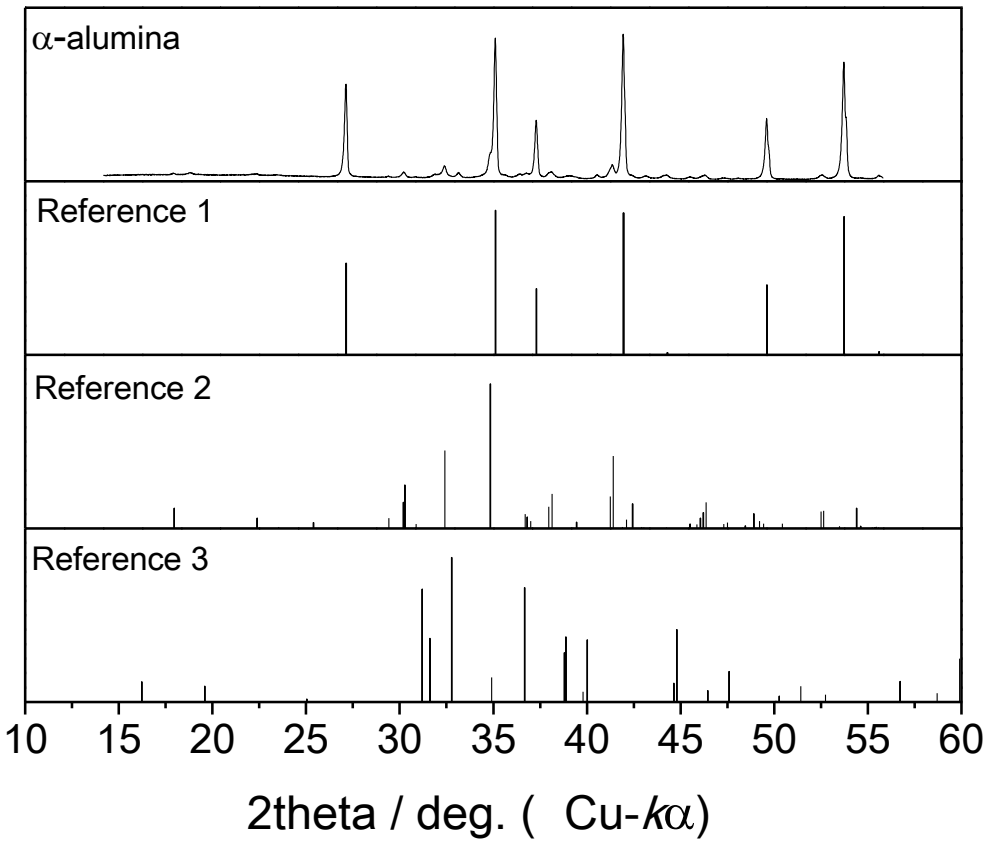

Figure S4. XRD patterns of α-Al_2O_3

Brief comments: The α-Al_2O_3 is indexed as a trigonal crystal system with space group $R\bar{3}c$. There are small amount of impurities of κ-Al_2O_3 (Orthorhombic, space group $Pna2_1$) and θ-Al_2O_3 (Monoclinic, space group $C2/m$).

[Reference 1, α-Al_2O_3] L. Lutterotti, P. Scardi, *J. Appl. Crystallogr.* **1990**, 23, 246.
[Reference 2, κ-Al_2O_3] L. smrcok, V. Langer, M. Halavarsson, S. Ruppi, *Z. Kristallogr.* **2001**, 216, 409.
[Reference 3, θ-Al_2O_3] E. Husson, Y. Repelin, *Eur. J. Solid State Inorg. Chem.* **1996,** 33, 1223.

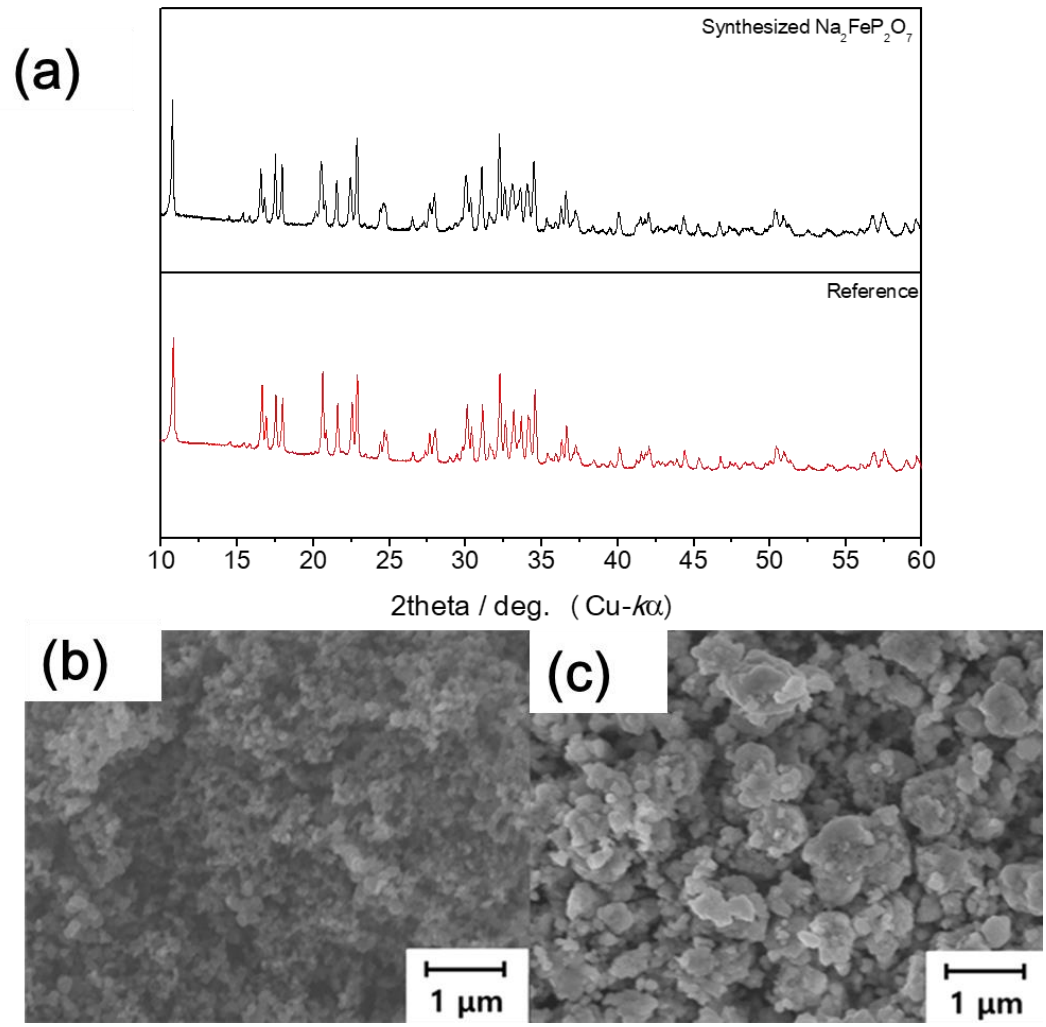

Figure S5. (a) XRD patterns of $Na_2FeP_2O_7$, and SEM images of electrodes (b) AB:PTFE, and (c) $Na_2FeP_2O_7$:AB:PTFE

Brief comments: The $Na_2FeP_2O_7$ is indexed as a triclinic crystal system with space group *P*-1 and patterns are consistent with the reference. The homogenous particle size of AB is confirmed in (b. The active material of $Na_2FeP_2O_7$ is evenly surrounded by AB with PTFE binder in (c).

[Reference] C.-Y. Chen, K. Matsumoto, T. Nohira, C. Ding, T. Yamamoto and R. Hagiwara, *Electrochim. Acta* **2014**, 133, 583.

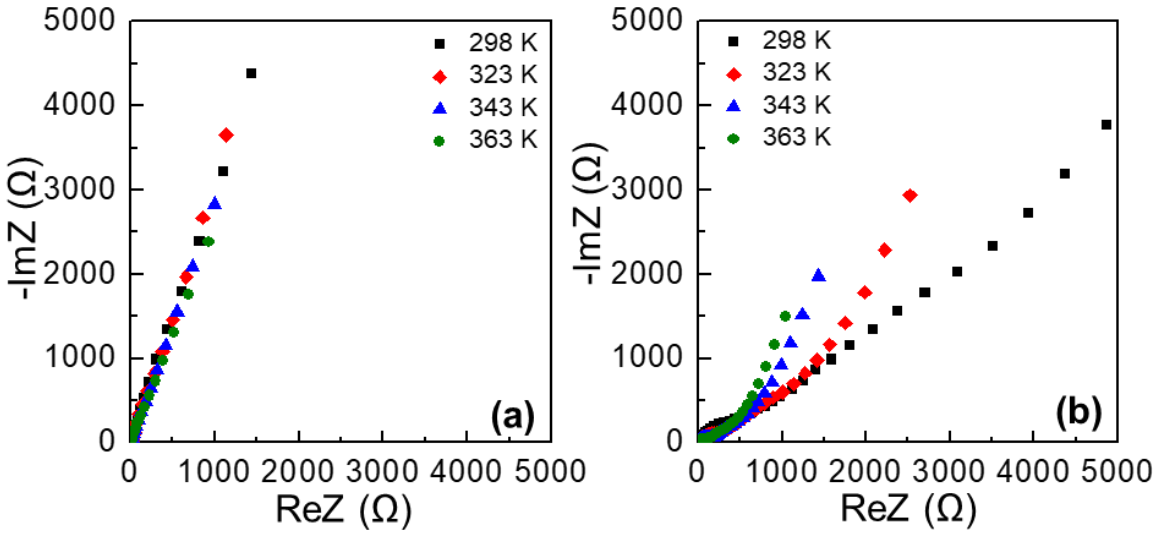

Figure S6 Nyquist plots for the $V_2O_5/IL_{FSA}/V_2O_5$ symmetric cells in the temperature range between 298–363 K. (a) V_2O_5:AB:PTFE = 75:20:5 wt% and (b) V_2O_5:PTFE = 95:5 wt%. Electrolyte: Na[FSA]-[C_2C_1im][FSA] (x(Na[FSA] fraction = 0.3), ac perturbation: 10 mV, frequency range: 10 mHz–100 kHz.

Brief comments: V_2O_5 (particle size: ~1μm) was selected as an electrode material at SOC 100% with a certain electronic conductivity. This is because, realistically, the fully desodiated state (SOC 100%) is difficult to establish from the electrode by starting from the discharged state (a very long constant current-constant voltage (CCCV) mode is required to extract Na^+ from the electrode). The seemingly large R_{ct} value supports the above-mentioned statement that, at SOC 100%, the Na^+ charge-transfer process does not occur.

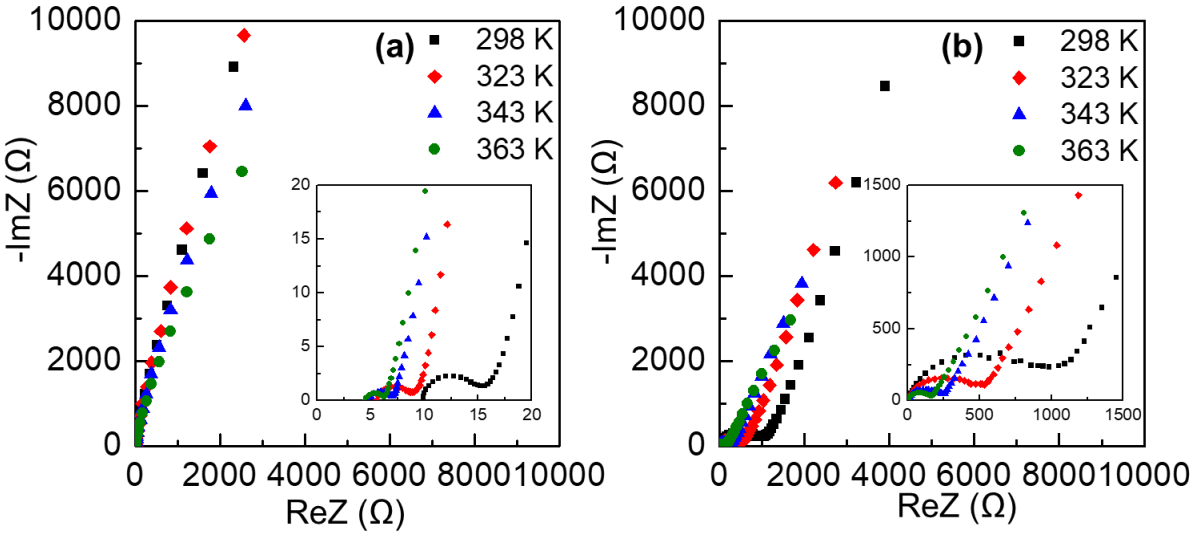

Figure S7. Nyquist plots for the $V_2O_5/IL_{FSA}/V_2O_5$ symmetric cells in the temperature range between 298–363 K for t(a) V_2O_5:AB:PVDF = 75:20:5 wt% and (b) V_2O_5:PVDF = 95:5 wt% and (inset) magnified plots. Electrolyte: Na[FSA]-[C_2C_1im][FSA] (*x*(Na[FSA] = 0.3), ac perturbation: 10 mV, frequency range: 10 mHz–100 kHz.

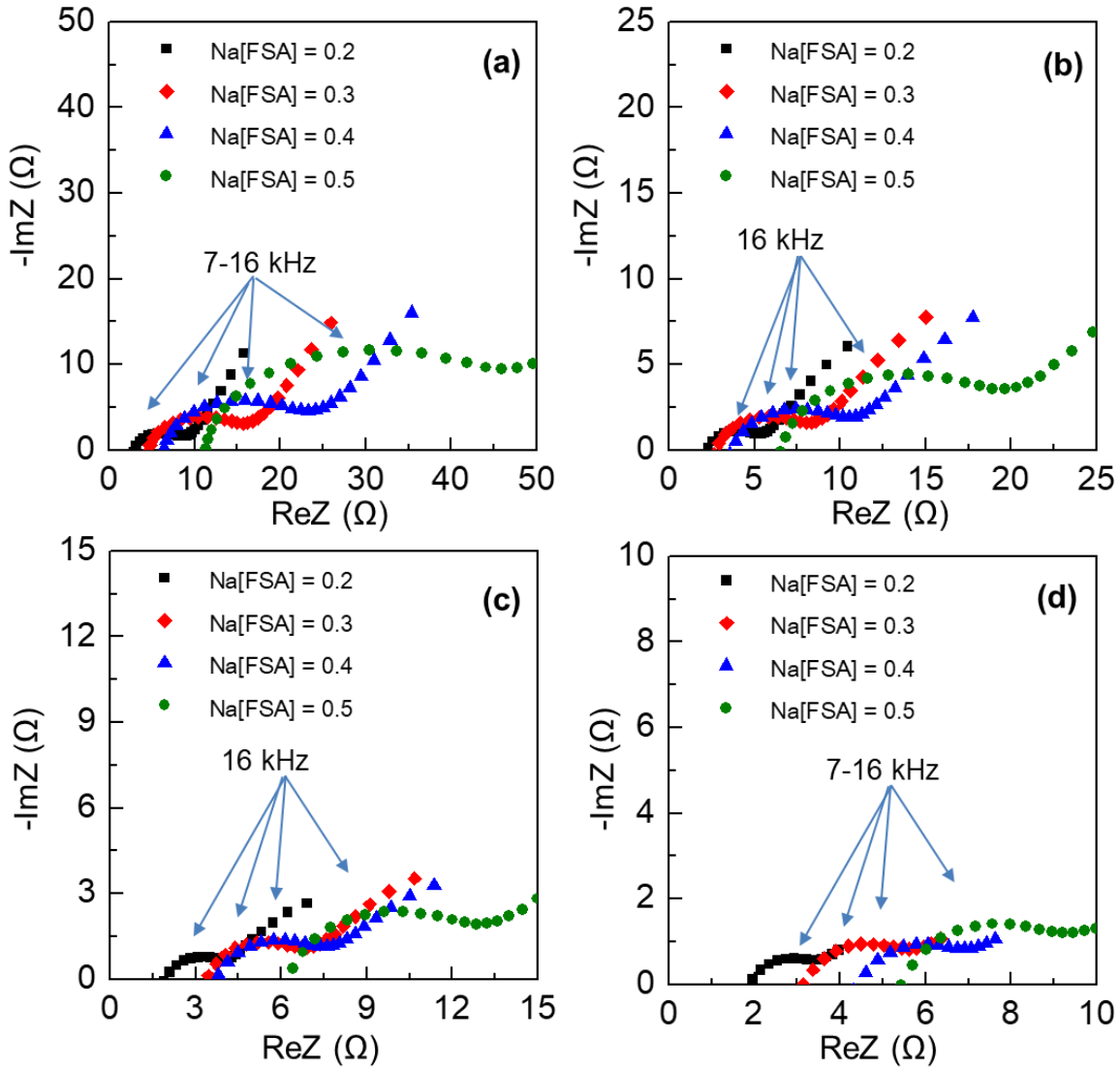

Figure S8. Nyquist plots for the $Na_2FeP_2O_7/IL_{FSA}/Na_2FeP_2O_7$ symmetric cells at (a) 298 K, (b) 323 K, (c) 343 K, and (d) 363 K at different scales. Electrolyte: Na[FSA]-[C_2C_1im][FSA], ac perturbation: 10 mV, frequency range: 10 mHz–100 kHz.